Pattern formation in a fully three-dimensional segregating granular flow

Mengqi Yu,[1] Paul B. Umbanhowar,[2] Julio M. Ottino,[1,2,3] and Richard M. Lueptow[2,1,3,*]
[1]*Department of Chemical and Biological Engineering, Northwestern University, Evanston, Illinois 60208, USA*
[2]*Department of Mechanical Engineering, Northwestern University, Evanston, Illinois 60208, USA*
[3]*Northwestern Institute on Complex Systems (NICO), Northwestern University, Evanston, Illinois 60208, USA*

(Received 20 October 2018; published 25 June 2019)

Segregation patterns of size-bidisperse particle mixtures in a fully three-dimensional flow produced by alternately rotating a spherical tumbler about two perpendicular axes are studied over a range of particle sizes and volume ratios using both experiments and a continuum model. Pattern formation results from the interaction of size segregation with chaotic regions and nonmixing islands of the flow. Specifically, large particles in the flowing surface layer are preferentially deposited in nonmixing islands despite the effects of collisional diffusion and chaotic transport. The protocol-dependent structure of the unstable manifolds of the flow surrounding the nonmixing islands provides further insight into why certain segregation patterns are more robust than others.

DOI: 10.1103/PhysRevE.99.062905

I. INTRODUCTION

Segregation of flowing granular materials, differing in properties such as density or size, has been studied both experimentally and theoretically in a number of canonical geometries including chutes [1,2], quasi-two-dimensional (quasi-2D) bounded heaps [3], and annular shear cells [4], where the underlying flow field is relatively simple and develops easily predicted segregation patterns. However, the situation can be more complex when the chaotic dynamics of the underlying flow field interacts with segregation, as can occur in quasi-2D tumblers [5–9]. Although chaotic flows have been well studied in fluids [10,11], similar studies with granular systems are few, particularly for three-dimensional (3D) systems.

As an example of the interaction between segregation and chaotic dynamics, consider the case of a quasi-2D tumbler with square cross section rotated at a constant speed [8], where nontrivial segregation pattern forms due to the competing influences of segregation and the underlying flow. Here, the tumbler is initially half-filled with a uniform mixture of small (diameter $d = 0.3$ mm) black glass particles and large ($d = 1.2$ mm) clear glass particles. The tumbler is rotated at constant angular speed ($\omega = 1.44$ rpm) so that particles continuously flow down the free surface (rolling or cascading regime [12,13]). After several revolutions, shown in Fig. 1(a), the small black particles accumulate in the two lobes, which extend from the core toward the two corners, while large clear particles occupy the periphery of the tumbler.

The lobed pattern comes from the time-periodic nature of the flow due to the tumbler geometry. That is, the surface flowing layer varies in length periodically from the position shown in Fig. 1(a) to a position where it spans the diagonal of the tumbler. The corresponding Poincaré section, a stroboscopic mapping [14] of points advected by a simple kinematic model of the granular tumbler flow, is shown in Fig. 1(b). The Poincaré section captures the time-periodic nature of the flow by recording the positions of points after each period (one quarter revolution). Some points in the Poincaré section are trapped in islands on the diagonals (closed loops), while others are advected throughout the domain [8]. The key point here is that the Poincaré section is based on a continuum model derived purely from the velocity field, without any information concerning the particles used in the experiments or their tendency to segregate. Nevertheless, the correspondence between the two nonmixing elliptic islands along the diagonals (evident as colored ellipses and associated lobes) in the Poincaré section and the lobes of small black particles in the experiment is clear. The segregation pattern is a manifestation of the interplay between segregation of particles in the flowing layer and the dynamics of the time-periodic flow in the tumbler. Initially, radial segregation drives small particles to the core of the bed of particles and large particles to the periphery of the tumbler. After the initial segregation, the large particles in the periphery of the tumbler experience chaotic advection of the flow field corresponding to the chaotic sea in the Poincaré section, while small particles in the core are subject to periodic dynamics of the nonmixing regions [8]. The underlying periodic dynamics interact with the segregation where the two processes overlap at the bottom of the thin surface flowing layer.

Pattern formation in quasi-2D tumblers occurs in many different tumbler geometries (square, pentagonal, triangular, and elliptical) with a range of particle types, sizes, weight fractions (2.5%–60%), tumbler fill fractions (50%–75%), and rotation rates [8,9]. In other situations, radial streaks of segregated particles as well as lobed patterns can be observed [5,7,8,15–18]. The streak pattern can coarsen [19] or become unstable, with streak locations changing with time. This behavior is thought to be driven by coupling of concentration and velocity in the flowing layer [5]. Time-periodic patterns have also been obtained in quasi-2D circular tumblers by a modulated angular velocity, which leads to a resonance in forcing [7]. Long streaks in a quasi-2D circular tumbler have been observed to occur after the initial radial segregation

*Corresponding author: r-lueptow@northwestern.edu

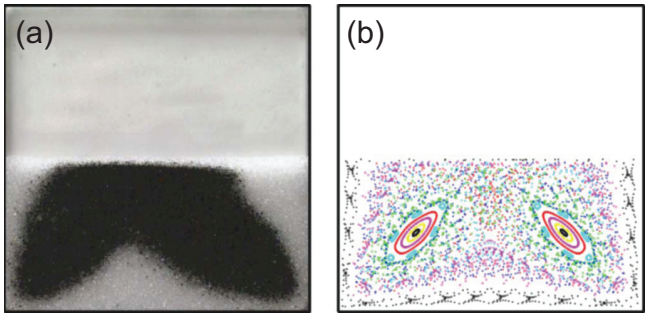

FIG. 1. (a) Segregation experiment in a half-full square tumbler with 40% small (0.3 mm) black particles and 60% large (1.2 mm) clear particles by weight. Steady-state pattern after ten clockwise revolutions of the tumbler at 1.44 rpm. (b) Poincaré section of a half-full square tumbler derived from model of flow kinematics. Reprinted with permission from Meier *et al.* [8].

and can be explained by an instability caused by variation in concentration of particles entering the flowing layer [16].

While the interaction between particle segregation in the quasi-2D square tumbler in Fig. 1(a) and the 2D chaotic dynamics of the associated Poincaré section based only on the kinematics of the flow is quite evident, it is not obvious if the same interaction will occur in a fully 3D system. Previous studies of granular flow in 3D tumblers focused on axial segregation in long rotating drums [15,20–22] and spherical tumblers [23–26]. It is only recently that chaotic dynamics in a spherical tumbler has been identified and a kinematic continuum model has been proposed [9,27,28]. In this paper, we examine whether or not granular segregation and chaotic dynamics interact in a similar way in a 3D system so as to generate segregation patterns related to nonmixing regions.

To answer this question, we consider segregation patterns in a 3D spherical tumbler that is half-filled with a mixture of small and large mm-sized spherical particles. As shown schematically in Fig. 2, the tumbler is rotated by angle θ_z about the z axis and then by angle θ_x about the x axis, where the z axis and x axis both lie in the horizontal plane. In the figure and in most previous studies, the axes are orthogonal, but in general, the angle γ between them can have any value [30,31]. This latter biaxial rotation protocol is specified by the triple $(\theta_z, \theta_x, \gamma)$ and typically is repeated many times. The segregation patterns described here depend on the specific protocol angles, mixture compositions, and particle sizes. There are other factors that can influence the segregation patterns such as particle density and tumbler wall smoothness, but they are beyond the scope of this study. Christov *et al.* [28] identified chaotic mixing regions coexisting with regular nonmixing islands based on a continuum model calculation of the underlying flow for certain protocols. An example of the coexisting chaotic region and nonmixing islands in the Poincaré section is shown in the bottom view of the system in Fig. 3(a), where the white elliptical regions (labeled A1–A3 and B1–B3) are nonmixing islands surrounded by the chaotic region covered in blue and red tracer points. This Poincaré section is calculated from the continuum model outlined in Christov *et al.* [28] by tracing points initially seeded on the interface between the bulk and the flowing layer (see Appendices A and B). The red and blue colors in the continuum

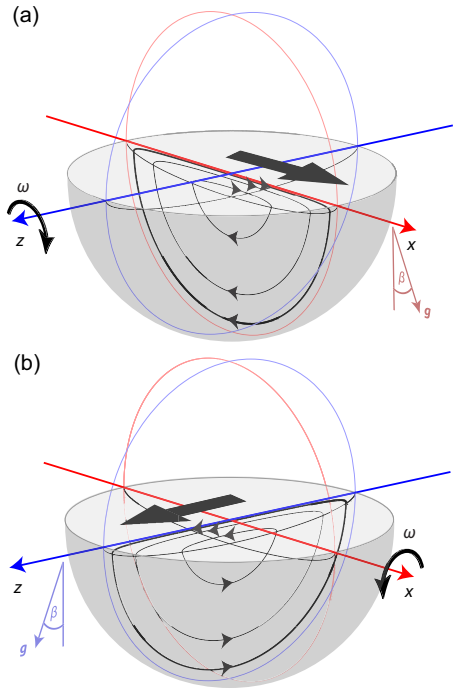

FIG. 2. Biaxial spherical tumbler flow consists of two alternating single-axis rotations about (a) the z axis and (b) the x axis, at a rotation speed ω. Material passing through the flowing layer (with a flat free surface at angle β to horizontal) is subsequently deposited downstream and then moves in solid-body rotation with the tumbler until it reenters the flowing layer. Reprinted with permission from Zaman *et al.* [29].

model indicate tracer points for the z-axis and x-axis rotations, respectively.

More recently, Zaman *et al.* [29] experimentally demonstrated that elliptic nonmixing islands in the flow of monodisperse particles serve as barriers to mixing by prohibiting material exchange across their boundaries. Specifically, they showed that a single tracer particle can stay within the nonmixing regions near the tumbler wall, periodically appearing in each of the period-3 nonmixing regions (either A1-A2-A3 or B1-B2-B3), over hundreds of iterations of the protocol in

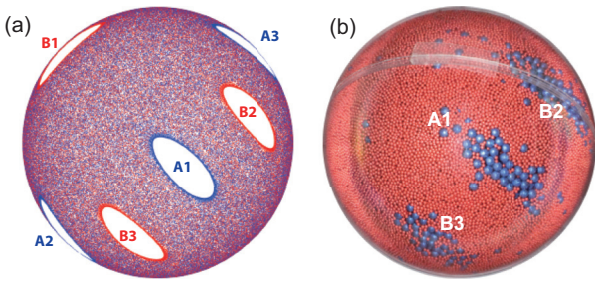

FIG. 3. (a) Bottom view of the Poincaré section of a half-full spherical tumbler for $r = 0.95$ with protocol (57°, 57°, 90°). (b) Bottom view of a segregation experiment in a half-full spherical tumbler with 15% large ($d = 4$ mm) blue particles and 85% small ($d = 1.5$ mm) red particles by volume with 30 iterations of the same protocol as in (a). Red and blue colors in experiments and in the continuum model are unrelated.

a spherical tumbler rotated about two orthogonal axes. Occasionally, the tracer particle wanders into the chaotic region due to collisional diffusion, but it eventually returns to the nonmixing regions where it can again remain hundreds more iterations. These nonmixing regions also can be predicted by the more abstract mathematical theory of piecewise isometries (PWI) [32,33], where discontinuities can generate complex dynamical behaviors as seen in various applications [34,35]. The PWI map, which applies to the limiting case of an infinitely thin flowing layer at the free surface [27,36,37], captures the skeleton of the underlying flow generated by the fundamental framework of cutting and shuffling, a mechanism for mixing discrete materials [27,29–31,38,39]. In this paper, we replace the monodisperse bed particles and single large tracer particle used in our previous work [29] with mixtures of small and large particles to explore if segregation patterns in a fully 3D system match the predictions of the Poincaré section derived from the flow kinematics alone. This would be analogous to the quasi-2D segregation pattern in Fig. 1(a) matching the 2D Poincaré section in Fig. 1(b). Apart from the fundamental question of whether 3D chaotic dynamics interact with granular segregation, this research has implications for practical devices for mixing granular materials in which nonmixing (segregation) regions are detrimental to the mixing process, a critical issue in mixing powders in the pharmaceutical and chemical industries.

The answer to the question of whether or not granular segregation and chaotic dynamics can interact in a 3D system to generate segregation pattern is immediately evident from the bottom view of an experiment with a mixture of initially mixed large blue particles ($d = 4$ mm) and small red particles ($d = 1.5$ mm) for protocol (57°, 57°, 90°), shown in Fig. 3(b), taken after 30 iterations. Large blue particles accumulate in the period-3 nonmixing regions at the bottom center of the tumbler, corresponding to A1, B2, and B3 islands in the Poincaré section in Fig. 3(a). The red and blue colors in the continuum model indicate tracer points for the z-axis and x-axis rotations, respectively. In the next section we will show that large blue particles also accumulate in the nonmixing regions labeled as A2, A3, and B1 on the periphery of the tumbler, which is not visible in Fig. 3(b) due to curvature of the tumbler surface.

Thus, it appears that the same mechanism that leads to pattern formation in the quasi-2D system of Fig. 1 also occurs in a fully 3D system. That is, segregation due to particle size difference effectively drives one particle species into the nonmixing features derived from dynamical system models. In the remainder of this paper we explore pattern formation in the 3D spherical tumbler, its relation to chaotic dynamics, and the details of the mechanisms that are involved.

II. SEGREGATION PATTERN VISUALIZATION

Experiments are conducted using the same apparatus and methodology described previously [29]. An acrylic spherical tumbler of diameter $D = 2R_0 = 14$ cm half-filled with mm-sized spherical glass particles is placed on an apparatus consisting of a set of three rollers mounted on a turntable. The spherical tumbler rests on the rollers, one of which is driven by a motor to rotate the tumbler about a single horizontal axis at 2.6 rpm. To rotate the tumbler about a different axis, a mechanism lifts the tumbler off the rollers, the turntable is rotated, and the tumbler is set back down on the reoriented rollers. In this way, the tumbler can be repeatedly rotated about two horizontal axes in an alternating fashion to perform a biaxial rotation protocol. In previous work [29], only a single large tracer particle was tracked. Here, we use a large number of larger diameter particles so that segregation patterns can form.

To qualitatively analyze the segregation pattern, we photograph the tumbler from below. After a desired number of biaxial rotations, the tumbler is removed from the apparatus, placed in a hole in a metal plate having a diameter slightly smaller than that of the tumbler, and photographed from below. Due to the curvature of the spherical tumbler, only the lower portion of the hemisphere is clearly captured in the photo [center circular image in Fig. 4(a)]. To view the periphery of the tumbler, a polished circular aluminum cylinder (15.2 cm diameter by 7.6 cm long) is attached to the bottom of the plate concentric with the tumbler. In this way, the reflection of the periphery of the tumbler is also captured in the photo [ring in Fig. 4(a)]. The tumbler is illuminated by a point LED light source positioned just to the side of the camera lens. Two photos are taken with the light source on the left and right sides of the camera lens while maintaining the same camera location and settings. The final image is obtained by combining left and right halves of the two photos that do not have glare or shadows. The light-colored arc above the label B2 in Fig. 4(a) is the seam between the two halves of the clear spherical tumbler.

Figure 4(a) shows pattern formation for the protocol (57°, 57°, 90°). Here, large blue particles accumulate in nonmixing regions surrounded by small red particles. There are six clusters of large blue particles, three in the center circle (A1, B2, and B3) and three reflected in the ring (A2, A3, and B1). These clusters align closely with the six nonmixing islands evident in the Poincaré section in Fig. 4(b), which is constructed according to the process outlined in Appendices A and B. The tumbler and the reflected ring in the Poincaré section are constructed using POV-Ray [40] in the same manner the tumbler is photographed in Fig. 4(a).

The similarity between the segregation pattern of clusters of large particles in Fig. 4(a) and the elliptic (nonmixing) regions in the Poincaré section in Fig. 4(b) is a key result of this paper. That is, the Poincaré section, which is based only on a simple kinematic model of the velocity in the flowing surface layer in the tumbler and has no particle segregation model at all, predicts the regions in which segregating particles (large particles in this case) accumulate. Thus, the chaotic dynamics of the system, as represented by the Poincaré section, predicts the segregation pattern for the experimental conditions.

Unlike the quasi-2D systems shown in Fig. 1, Poincaré sections in a fully 3D systems are three dimensional. Figures 3 and 4 only show the segregation pattern visible at the clear wall of the spherical tumbler and the corresponding Poincaré section at a dimensionless radius of $r = 0.95$ (just adjacent to the wall of the tumbler). These 2D nonmixing islands on different invariant surfaces form a 3D structure around a line of periodic points [9,28,41–43]. To visualize the 3D structure in the spherical tumbler flow, trajectories of the points on the boundaries of nonmixing islands for the (57°, 57°, 90°)

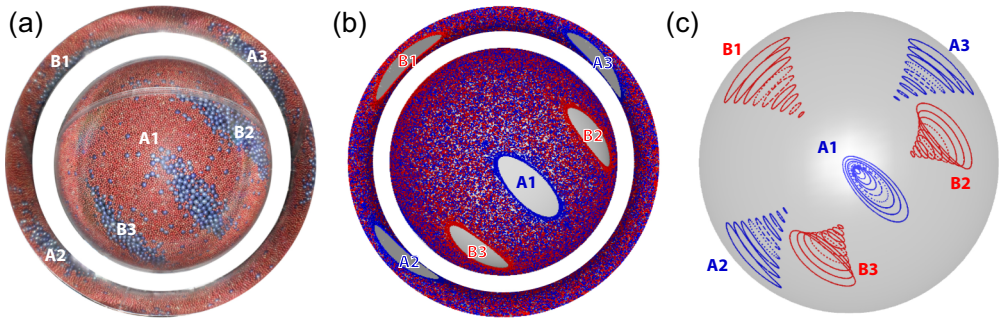

FIG. 4. (a) Segregation experiment in a half-full spherical tumbler rotated at 2.6 rpm with 10% large blue particles (3 mm) and 90% small red particles (1 mm) by volume showing six distinct large particle islands after 30 iterations of protocol (57°, 57°, 90°). The outer ring is the tumbler reflection in the surrounding cylinder, which shows the periphery of the tumbler. (b) POV-Ray [40] generated view of Poincaré section including a reflective cylinder. Flowing layer edges are tracked for 500 iterations near the tumbler wall at nondimensional radius $r = 0.95$. (c) Bottom view of 3D nonmixing islands from continuum model for $0.55 < r < 0.95$ in increments of 0.05 consist of a pair of period-3 islands for a total of six conical-shaped nonmixing structures (A1-A2-A3 and B1-B2-B3).

protocol in the radius range of $0.55 < r < 0.95$ are isolated and assembled in Fig. 4(c) to form six conelike Kolmogorov-Arnold-Moser (KAM) tubes [28,42], analogous to 2D KAM islands. The shape of the 3D KAM structure is determined by the protocol. The 3D KAM structures shown here for the (57°, 57°, 90°) protocol are conical with their apex pointing toward the center of the hemisphere. The bases of the conelike KAM tubes are at the wall of the tumbler and correspond to the islands A1–A3 and B1–B3 in which the large particles accumulate in Fig. 4(a). Viewing the hemisphere from the bottom as in Fig. 4(c), the A2, A3, and B1 KAM tubes are viewed from the side making their conical shape obvious, while the A1 KAM tube is viewed from its base [leading to the nested ellipses in Fig. 4(c)]. KAM tubes B2 and B3 are between these extremes of orientation. The largest ellipse in each of the six KAM tubes, which is the portion of the KAM tubes closest to the wall of the tumbler, corresponds to the elliptical nonmixing regions in Figs. 4(a) and 4(b).

In Fig. 4(a), the mixture consists of 10% large (3 mm) blue particles and 90% small (1 mm) red particles. The large blue particles accumulate into regions that correspond to nonmixing islands predicted by the continuum model. To fully characterize the pattern formation, experiments are carried out across a range of particle size ratios R and large particle volume fractions f. Figure 5 shows experimental results for mixtures of equal-density spherical glass particles with actual particle size ratios 3.56, 2.67, 2.1, 1.27, and 1.69. Nominal and actual particle diameters of the mixtures used in the experiments are listed in Table I. The volume fraction of large particles is 5%, 15%, and 25%. In the first four columns of Fig. 5, the large particle size is kept constant at 4 mm to allow a direct visual comparison of the coverage of large particles on the tumbler wall. The rightmost column with $R = 1.69$ and a large particle diameter of $d = 2$ mm provides a comparison to size ratio $R = 2.1$ images with large particle diameter of $d = 4$ mm to assess the effect of the tumbler size relative to particle sizes.

Consider the first row of experiments with $f = 5\%$. The three clusters of blue particles match with nonmixing islands A1, B2, and B3 predicted by the Poincaré section calculated from the continuum model in Fig. 4(b). The boundaries of the regions of blue particles become more difficult to discern as the particle size ratio decreases, particularly for $R = 1.27$. This result is expected since a smaller size ratio reduces segregation. Consequently, particles have a greater tendency to remain in a mixed state, resulting in less distinct segregation with a smaller size ratio. It is also evident that the islands of large blue particles are smaller for larger size ratios. This is likely a result of the relatively small fraction of large particles and the large particle size ratio, which allows small particles to populate regions at the wall below the large particles.

As the volume fraction of large particles increases (rows two and three in Fig. 5), the same segregation pattern persists. For all size ratios, the clusters of large particles occupy larger area as f increases from 5%–25%, growing in both length and width, because more large particles are available to accumulate in the nonmixing regions. In general, accumulation of large particles into the nonmixing regions is more distinct with a larger size ratio, while collisional diffusion and segregation make the patterns less evident with decreasing size ratio so that for a size ratio of $R = 1.27$ and $f = 25\%$ the segregation pattern is no longer evident.

For the four size ratios on the left in Fig. 5, the large particle diameter remains constant at 4 mm while the small particle size varies. Consider now the size ratio $R = 1.69$ in Fig. 5, where the large particle size is now 2 mm instead of 4 mm. The accumulation of large blue particles into three nonmixing regions is still observed across the different large particle

TABLE I. Nominal particle sizes and corresponding actual particle sizes.

Color	Red				Blue	
Nominal size (mm)	1	1.5	2	3	2	4
Actual size (mm)	1.12 ± 0.09	1.50 ± 0.13	1.90 ± 0.09	3.15 ± 0.14	2.03 ± 0.12	3.99 ± 0.04

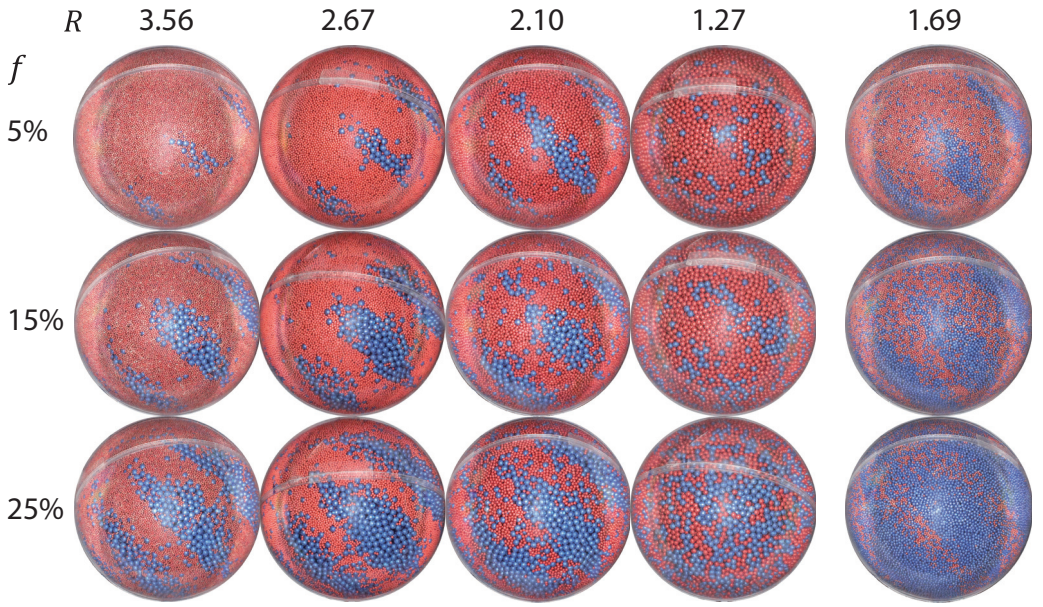

FIG. 5. Segregation experiments in a half-full spherical tumbler after 30 iterations of protocol (57°, 57°, 90°) rotated at 2.6 rpm for a range of mixtures: 5%, 15%, and 25% volume fraction f of large blue particles with small red particles, for size ratios $R = 3.56$, 2.67, 2.1, 1.27, 1.69. All columns use 4 mm diameter large particles except for the rightmost column where the large particle diameter is 2 mm.

volume fractions. At $f = 25\%$, compared with a similar size ratio $R = 2.1$, the coverage of large blue particles is much higher with fewer small red particles visible. Yet, it is still obvious that large blue particles accumulate more intensely in the nonmixing regions.

The series of experiments in Fig. 5 demonstrates that the segregation pattern for this particular protocol (57°, 57°, 90°) is quite robust and manifests itself across a wide range of particle size ratios and large particle volume fractions, despite the interplay between collisional diffusion and segregation due to particle size difference. The segregation pattern becomes clear after about 15–20 iterations and remains obvious with more iterations (see Fig. S1 in the Supplemental Material for experiments at 20, 40, and 50 iterations). The protocol (57°, 57°, 90°) exhibits robust and repeatable patterns with every run (see Fig. S2 in Supplemental Material for repeated experiments, the average of which overlays the corresponding image in Fig. 5 almost exactly). The period-3 nonmixing structures in protocol (57°, 57°, 90°) segregation pattern are not unique. More generally, similar period-3 segregation patterns also develop after 15–20 iterations for a range of rotation angles (54°–60°) about both axes (see Fig. S3 in Supplemental Material [44] for segregation experiments of protocol (54°, 54°, 90°) and (60°, 60°, 90°) and a comparison to corresponding Poincaré sections).

Collisional diffusion tends to disperse particles throughout the domain, as is evident from weaker segregation at smaller R. In previous work on spherical tumbler flow, chaotic advection also drives particles across the entire domain with random paths [29]. Thus, we hypothesize that the segregation between large and small particles traps many large particles in the nonmixing regions resulting in the pattern formation. The details of the features depend on the relative strength of diffusion, segregation, and chaotic advection, which is also observed in the structure variation (stratified, segregated, and mixed states) of bounded heap flows [45]. Other factors including rotation rates and fill fractions may also influence pattern formation in a quasi-2D tumbler [5,8], and are likely to do so in a spherical tumbler.

III. NONMIXING STRUCTURES IN 3D

Visualization of the segregation patterns formed at the tumbler wall in the previous section is an intuitive way to qualitatively analyze the pattern formation, but only near the tumbler wall. As shown in Fig. 4(c), the nonmixing structures predicted by the Poincaré section are cone-like in three dimensions. Hence, x-ray imaging is employed to examine the 3D nature of particle segregation.

The x-ray imaging equipment used in this study is the same as used previously [29]. X-ray images of the tumbler are captured by a detector located below the tumbler apparatus as shown in the schematic in Fig. 6. The 14 cm diameter tumbler appears as a circular image on the detector with a diameter of 612 pixels. The image is calibrated to remove warping effects in image detection due to the image intensifier and camera optics [29]. The tracer particle used in this study is about 3 mm in diameter, which is about 13 pixels in the image. The coneshaped x-ray beam makes it possible to obtain the 3D positions of multiple tracer particles as follows. When the tumbler is slowly rotated to the granular material's angle of repose and back, all particles move in solid body rotation. A sequence of images are taken at one frame per angle of rotation to record the positions of all tracer particles. Then, the 3D trajectories of tracer particles can be tracked. These trajectories project onto the detector image at different trajectory lengths depending on the particle depth, as shown in the schematic side view in Fig. 6. For example, the black particle that is closer to the tumbler wall has a longer projected trajectory (l_2) than that of the red particle (l_1), which is located

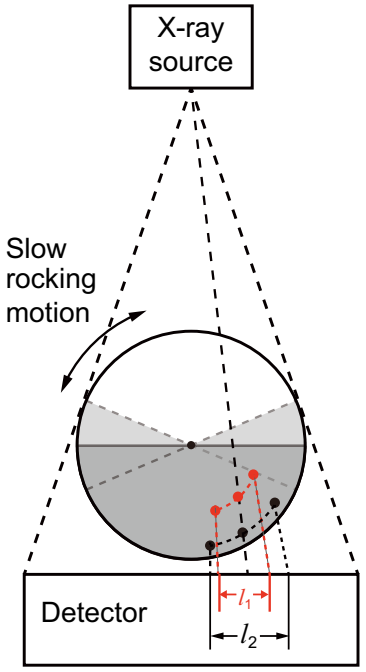

FIG. 6. Schematic of depth determination. Cone-shaped x-ray beam passes through the tumbler and x-ray images are captured by a detector below the tumbler. Rotating the tumbler between the two extremes defined by the repose angle results in trajectories l_1 and l_2 at the detector that depend on the radial location of the particle in the tumbler.

farther radially inward. However, the tracer particle positions are projection-distorted because the x rays that strike the flat detector traverse different distances depending on the depth of the particle and how far it lies from the source-detector central axis. The 3D position of a tracer particle can be calculated iteratively from the sequence of 2D images during the slow rotation where all particles move in solid body rotation (a rocking motion). Based on the tracer particle coordinates in the images, an approximate radial location of the particle in the tumbler can be determined. With the estimated radius, coordinates of the trajectory are adjusted accordingly, and a new value of the radius can be calculated. This process is repeated until the difference in radius between successive iterations is less than 1%. With multiple tracer particles, a particle tracking velocimetry (PTV) algorithm in MATLAB is used to detect and trace particle trajectories [46]. To ensure accurate tracking, only trajectories longer than 65% of the sequence length are used, which also reduces error due to particles overlapping. In this way, the 3D position of many x-ray opaque tracer particles is obtained after each rotation of the protocol.

The apparatus and analysis methods have some limitations. Tracking the trajectories of tracer particles requires accurate detection of the particles in the x-ray image. With a large number of tracer particles, particles often overlap in the x-ray image. Particles at different depths may be projected to the same neighborhood on the detector image, particularly as particles accumulate into a nonmixing region and overlap. At the same time, when the tumbler is rotated to the angle of repose, the relative particle locations change, so that particles

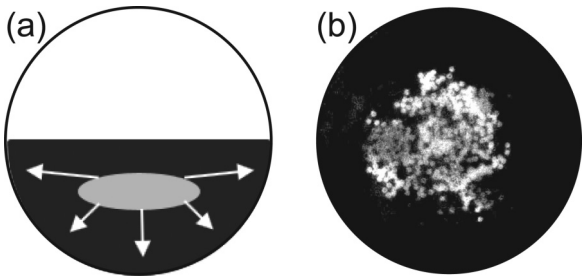

FIG. 7. Initial condition for tracking particles segregating toward the tumbler wall. Large x-ray opaque 3 mm silver particles (gray region) are seeded in the core of the hemispherical bed of 1.8 mm glass particles (black background) as shown in (a) a side view schematic with arrows indicating that these particles are expected to segregate toward the tumbler wall and (b) a bottom-view x-ray image.

may cross over each other or overlap in the images. Thus, it is challenging to track a large number of particles. To avoid inaccurate detection of particles, experiments are limited to fewer than 200 x-ray opaque tracer particles. With 3 mm particles, this comprises less than 1% of the total particle volume. Thus, for experiments with volume fractions of large particles higher than 1%, both large x-ray opaque tracer particles and large glass beads of similar density are used to provide the appropriate volume of large particles. Nevertheless, the tracer particles still represent the ensemble behavior of all large particles.

The continuum model for the $(57^\circ, 57^\circ, 90^\circ)$ protocol predicts conelike nonmixing structures, each with its base on the wall of the spherical tumbler and its apex pointing toward the center of the tumbler [Fig. 4(c)]. The conelike nonmixing structure narrows to the size of a typical large particle at a dimensionless radius of about $r = 0.55$. If the particle is larger than the KAM tube, a single particle in a nonmixing region cannot be distinguished from particles dispersed randomly in the chaotic region. Therefore, nonmixing structures in the experiment should only occur for locations in the tumbler where $r > 0.55$. We use this result to explore how particles segregate and patterns form in the tumbler. Two experiments tracking x-ray opaque tracer particles are performed, first targeting particles that start near the center of the bed that should segregate to near the tumbler wall and accumulate in nonmixing regions, and second, targeting particles that start near the tumbler wall that should segregate toward the center of the tumbler where the conelike nonmixing regions do not extend.

In the first experiment, 400 $d = 3.01 \pm 0.04$ mm, $\rho = 2.5 \pm 0.05\,\mathrm{g\,cm^{-3}}$ hollow silver jewelry beads (Beadcorp) with 0.9 mm holes are used as x-ray tracer particles with $d = 1.84 \pm 0.07$ mm $\rho = 2.45 \pm 0.3\,\mathrm{g\,cm^{-3}}$ glass particles in the bulk. The tracer particles are seeded in the core of the tumbler [Fig. 7(a)], appearing as a circular cluster in the bottom-view x-ray image [Fig. 7(b)]. Thus, the initial blob of large x-ray opaque tracer particles starts at a radial location near the apices of the conical nonmixing structures. Once the rotation protocol starts, the large x-ray opaque particles should migrate to near the wall of the tumbler due to segregation in the flowing layer, recalling that larger particles preferentially segregate to the surface of the flowing layer and thereby to

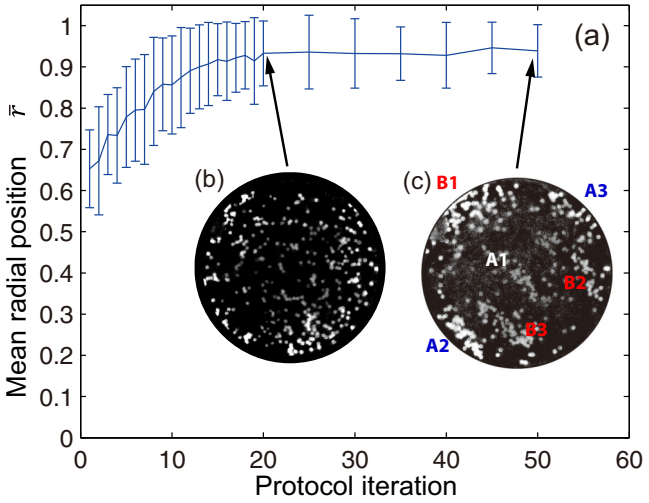

FIG. 8. (a) Mean normalized radius $\bar{r}$ of large x-ray opaque tracer particles vs. protocol iterations for protocol (57°, 57°, 90°). X-ray images of tracer particles at (b) 20 iterations and (c) 50 iterations. Particles have segregated to near the tumbler wall after 20 iterations, but only at 50 iterations are the tracer particles segregated into nonmixing islands labeled by A1-A2-A3 and B1-B2-B3. Error bars are + or − one standard deviation.

the periphery of the bed of particles [47]. The question is: Do the large particles accumulate in nonmixing regions before or after they get near the tumbler wall?

To answer this question, in this experiment, after each iteration, the 3D positions of all tracer particles are obtained. The mean tumbler-radius normalized radial position $\bar{r}$ of tracer particles in the tumbler is calculated to quantify the extent of the segregation. In Fig. 8(a), the mean normalized radius of tracer particles $\bar{r}$ is plotted against the number of iterations. The mean radius starts around 0.7, increases rapidly in the first 20 iterations, and then stays fairly constant at about 0.9. Thus, the tracer particles segregated to near the wall of the tumbler, as expected. At 20 iterations [Fig. 8(b)], tracer particles are dispersed randomly throughout the image but are near the tumbler wall based on Fig. 8(a). After 50 iterations [Fig. 8(c)], tracer particles form clusters in the nonmixing regions as predicted by the continuum model, labeled as A1-A2-A3 and B1-B2-B3. Note that the intensity of Fig. 8(c) is adjusted using adaptive histogram equalization in MATLAB (ADAPTHISTEQ) [48,49], where the contrast is enhanced in 64 smaller tiles across the entire image. The clusters form slowly, becoming more evident toward the end of the experiment. This result demonstrates that large particles accumulate in nonmixing regions consistent with the continuum model but only after they have first segregated to near the wall of the tumbler where the nonmixing regions have significant volume due to their conical shape.

In the second experiment we use a mixture of 400 $d = 3.01 \pm 0.04$ mm hollow silver jewelry beads ($\rho = 2.5 \pm 0.05\,\mathrm{g\,cm^{-3}}$) as tracers with $d = 1.92 \pm 0.04$ mm acrylic particles ($\rho = 1.24 \pm 0.08\,\mathrm{g\,cm^{-3}}$) in the bulk. This combination of size and density differences causes the silver particles to sink to the bottom of the flowing layer during tumbler rotation while the acrylic particles rise to the surface of the flowing

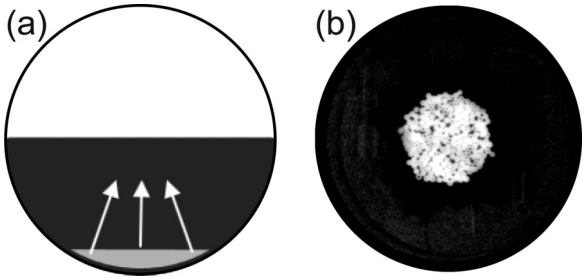

FIG. 9. Large silver particles (3 mm) are seeded at the bottom of the hemispherical bed of 2 mm acrylic particles as shown in (a) the side view schematic with arrows indicating that these particles are expected to segregate toward the center of the particle bed and (b) a bottom-view x-ray image.

layer so they segregate toward the tumbler wall. The silver particles are seeded at the bottom of the tumbler as shown in the side view and bottom view in Figs. 9(a) and 9(b), respectively. Since silver particles sink to the bottom of the flowing layer, they are expected to segregate toward the core of the hemispherical bed of acrylic particles as the tumbler is rotated. The mean normalized radius of silver particles is plotted as a function of the number of protocol iterations in Fig. 10(a). Due to difficulties detecting the silver particles in the first few iterations, a dashed line is drawn to connect the initial condition (particles deposited at the tumbler wall) to subsequent iterations. The mean radius drops quickly to below 0.7 in the first 20 iterations and does not vary significantly afterwards. The x-ray images at 20 iterations [Fig. 10(b)] and 50 iterations [Fig. 10(c)] both show x-ray opaque silver tracer particles in the middle portion of the tumbler, meaning that tracer particles relocate from near the tumbler wall to the core of the bed of particles. The dispersion of particles at 50 iterations is very similar to that at 20 iterations, and there is no apparent structure or accumulation of large particles other than near the core of the bed of particles. This result again

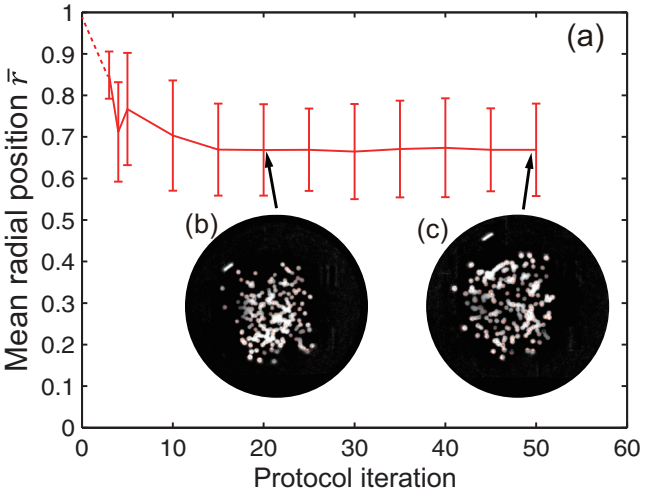

FIG. 10. (a) Mean normalized radius $\bar{r}$ of x-ray opaque tracer particles vs. number of protocol iterations (57°, 57°, 90°). X-ray image of tracer particles at (b) 20 iterations and at (c) 50 iterations. Error bars are + or − one standard deviation.

TABLE II. Mean normalized radius $\bar{r}$ and standard deviation of normalized radius σ_r of tracer particles over 46–50 iterations of experiments with a mixture of 3 mm large silver tracer particles and glass particles and 1 mm small glass particles with large particle volume fractions $f = 5\%$, 15%, and 25%.

f	5%	15%	25%
$\bar{r}$	0.9446	0.9358	0.9257
σ_r	0.0629	0.0575	0.0816

matches the prediction of the continuum model [Fig. 4(c)], where no significant nonmixing structures exist near the core of the particle bed.

This pair of experiments demonstrates that particles form the segregation pattern predicted by the continuum model only close to the tumbler wall. The transport of particles can also be tracked as the volume fraction of large particles increases. Similar size and density glass beads ($d = 3.15$ mm, $\rho = 2.45\,\mathrm{g\,cm^{-3}}$) are used along with 200 silver tracer particles ($d = 3.01$ mm, $\rho = 2.5\,\mathrm{g\,cm^{-3}}$) to make total large particle volume fractions $f = 5\%$, 15%, and 25% mixtures with 1 mm small glass particles. Since the large glass beads and tracer particles have similar size and density, the behavior of tracer particles mirrors the bulk behavior of all large particles. The tracer particles are tracked for 50 iterations of the $(57^\circ, 57^\circ, 90^\circ)$ protocol with large particles initially seeded in the center of particle bed. The mean normalized radius of tracer particles for all volume fractions decreases only slightly with increasing large particle volume fraction, at steady state (46–50 iterations), as shown in Table II.

The results in Table II are consistent with the nonmixing regions expanding in size at the tumbler wall with increasing large particle volume fraction, as is evident in Fig. 5. However, the slight reduction in the mean normalized radius in Table II suggests not all large particles are in the monolayer at the wall. Based on approximating the coverage of a monolayer of large particles at the tumbler wall, we estimate that most large particles are within three particle diameters of the wall at the higher larger particle volume fractions. Thus, the large particles do not entirely occupy the conical nonmixing structures predicted by the continuum model in Fig. 4(c) but tend to expand the regions of large particles near the tumbler wall. This indicates that the mechanism of pattern formation is closely related to the segregation dynamics that occurs in the flowing layer.

The effect of segregation may be so strong that large particles are pushed to the surface of the flowing layer so they never have a chance to fill the subsurface volume of the conelike nonmixing structures. On the other hand, when segregation is weak, particles tend to mix more uniformly instead of accumulating in the nonmixing structures as occurs for $R = 1.27$ in Fig. 5. Large particles at this size ratio may disperse more uniformly in the domain and experience a weaker tendency to segregate, which may allow them to extend farther toward the apex of the nonmixing structures. Likewise, rotating the tumbler at a higher angular speed results in a thicker flowing layer that may similarly enable large particles to further fill the conical nonmixing structures. Additional quantitative analysis requires data of precise positions and velocities, which can be obtained from discrete element method simulations that are currently underway.

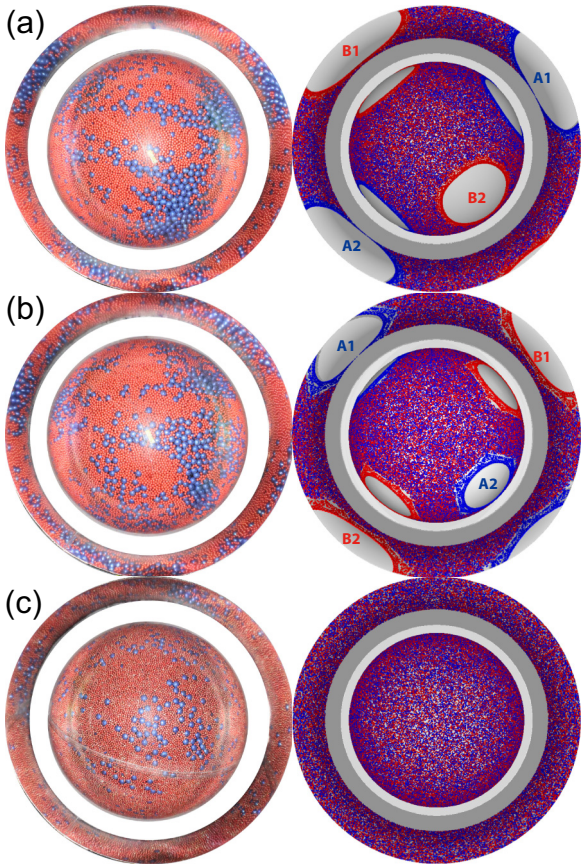

FIG. 11. Experiments (left) compared to Poincaré sections (right) after 30 iterations of protocol $(90^\circ, 90^\circ, 80^\circ)$ in (a), $(90^\circ, 90^\circ, 90^\circ)$ in (b), and $(75^\circ, 60^\circ, 90^\circ)$ in (c). Visualization of tumbler wall for corresponding experiments with 15% large blue particles (4 mm) and 85% small red particles (1 mm).

IV. DEPENDENCE ON ROTATION PROTOCOLS

Similarity between the pattern formation in experiments and nonmixing regions in the continuum model can be demonstrated in several other protocols, including those shown in Fig. 11: $(90^\circ, 90^\circ, 80^\circ)$, $(90^\circ, 90^\circ, 90^\circ)$, and $(75^\circ, 60^\circ, 90^\circ)$. Large blue particles accumulate in two pairs of period-2 nonmixing islands labeled as A1-A2 and B1-B2 in Fig. 11(a) for protocol $(90^\circ, 90^\circ, 80^\circ)$. Note that here the two rotation axes are not orthogonal, but at an angle of 80°. Similarly for the orthogonal axes case $(90^\circ, 90^\circ, 90^\circ)$, large blue particles also accumulate into period-2 nonmixing islands despite more particles appearing in the chaotic region between the nonmixing islands. The period-2 nonmixing structures also occur in combinations of a range of rotation angles α and β with different angles between axes γ (see Fig. S4 in Supplemental Material for experiments of protocols also exhibiting period-2 nonmixing structures). For the protocol $(75^\circ, 60^\circ, 90^\circ)$ [Fig. 11(c)], where no nonmixing structures are predicted by the continuum model, the experiment shows no clear segregation patterns, as expected. Consequently, we speculate

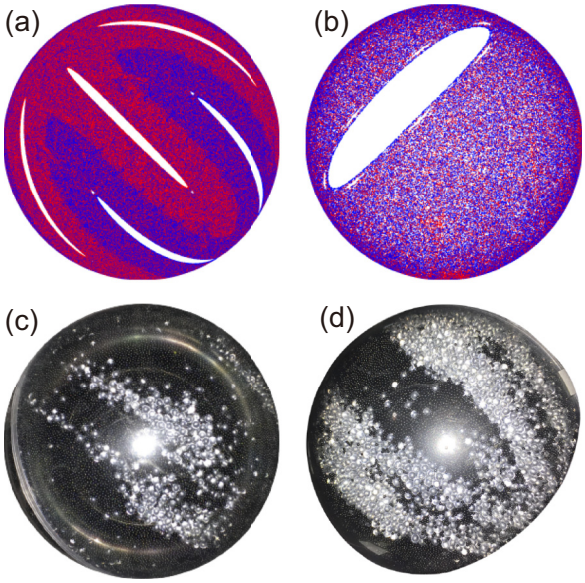

FIG. 12. Poincaré section of the continuum model in (a) the bottom view of the bulk and (b) the bottom view of the flowing layer for protocol (45°, 45°, 90°). Segregation patterns after 30 iterations in a half-full spherical tumbler with 10% large clear particles (3 mm) and 90% small black particles (1 mm) starting with (c) large particles in the bottom of tumbler (bottom view), and (d) large particles on top of the flowing layer.

that other protocols that exhibit large nonmixing regions will show associated segregation regions in experiments.

The nonmixing islands for protocols (57°, 57°, 90°), (90°, 90°, 80°), and (90°, 90°, 90°) are called persistent [29] in that they correspond to cells in PWI maps [36,37], which provide a mathematical description of the action of cutting and shuffling that forms the foundation for nonmixing regions in spherical tumbler flow with alternating rotations about two axes [29]. Although PWI maps assume a nonphysical infinitely thin flowing layer at the surface, the nonmixing structures they generate can persist for a finite-thickness flowing layer [29], as is evident in these experiments. The boundaries of the nonmixing islands are defined by the interface between the flowing layer and the bulk [29,37].

In addition to the persistent nonmixing regions described thus far, there is another type of barrier to mixing known as an emergent nonmixing region [29], which is not present in the PWI map but emerges in the continuum model for a finite flowing layer thickness. Unlike persistent nonmixing regions that pass entirely through the flowing layer with each rotation and have boundaries set by the boundary of the flowing layer, emergent nonmixing regions periodically land entirely within the flowing layer, are stretched in the streamwise direction, and have boundaries that are not necessarily coincident with the flowing layer boundary [29]. For a detailed discussion of persistent and emergent nonmixing islands, see Zaman *et al.* [29]. An example of a Poincaré section exhibiting emergent nonmixing islands is shown in Figs. 12(a), 12(b) for protocol (45°, 45°, 90°). The Poincaré section consists of interpenetrating fingers that are primarily red or primarily blue when viewed from the bottom [Fig. 12(a)]. The boundaries between the red and blue regions are shown to be barriers to mixing [29]. The stretching of one of the white nonmixing regions at the centers of the interpenetrating fingers is evident in Fig. 12(b), which shows a nonmixing region as visualized from below as it lands entirely in the flowing layer between rotations.

To examine the influence of emergent nonmixing islands on segregation, experiments are conducted with the protocol (45°, 45°, 90°) for a mixture of 10% large clear glass particles ($d = 2.97 \pm 0.05$ mm) with 90% small black glass particles ($d = 1.05 \pm 0.05$ mm) with two different initial conditions: large particles initially located in the bottom of the tumbler on the tumbler wall and large particles initially spread on top of the flowing layer. For the first experiment, large particles initially located at the bottom on the tumbler wall, accumulate into three pairs of thin strips, with the most visible pair in the middle [Fig. 12(c)]. This pattern corresponds to the red fingers in the continuum model [diagonal from top left corner to bottom right corner and on the left and upper periphery in Fig. 12(a)] with a thin nonmixing region in the middle of the fingers. The nonmixing region (white) in the middle of the diagonal finger [Fig. 12(a)] corresponds with the central small black particle filled region in Fig. 12(c). In the second experiment [Fig. 12(d)], large particles initially located in the flowing layer accumulate in the two visible blue fingers of the Poincaré map, again with the central nonmixing region (white) filled with small black particles [a third blue finger is stretched across the flowing layer, consistent with Fig. 12(b)]. This result is expected since the blue finger is mapped onto the flowing layer where large particles initially are located [Fig. 12(a)]. In both experiments, large particles do not occupy the white nonmixing regions predicted by the continuum model. Instead they accumulate in the colored fingerlike structures, demonstrating that the mixing barriers between the red and blue dominant regions in the continuum model are physical mixing barriers preventing material exchange [29]. Particles starting in one region are mostly confined in this region even with collisional diffusion. For all of the protocols in this section, the experiments demonstrate robust pattern formation matching features in the Poincaré sections derived from the continuum model.

V. MECHANISM OF PATTERN FORMATION

A. Pattern formation in three dimensions versus quasi-two-dimensions

At first glance, segregation pattern formation in quasi-2D tumblers and 3D spherical tumblers appear similar. In the flowing layer, particles segregate due to differences in size, and at steady state one species accumulates in the predicted nonmixing islands while the other species occupies the rest of the domain. However, a major difference is that large particles occupy the chaotic region in a quasi-2D tumbler, while they accumulate in persistent nonmixing structures in a 3D spherical tumbler. Conversely, small particles accumulate in the nonmixing region in a quasi-2D tumbler, while they occupy the chaotic region in a 3D spherical tumbler.

To explain this difference, first note that segregation in the flowing layer occurs in the same manner in both quasi-2D and 3D spherical tumbler geometries. Small particles percolate

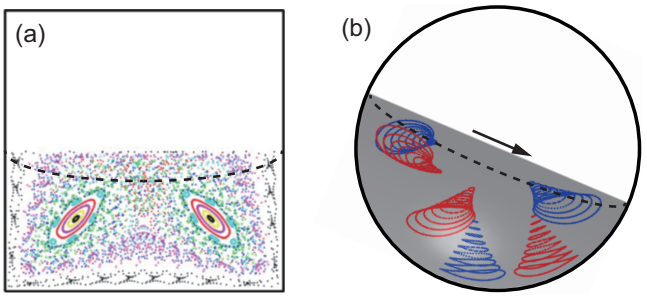

FIG. 13. Schematic of the boundary of the flowing layer (dashed curve) superimposed onto the Poincaré section for (a) a half-full quasi-2D square tumbler and (b) a half-full 3D spherical tumbler.

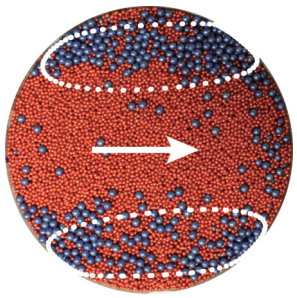

FIG. 14. Top view of the flowing layer in a tumbler half-filled with 15% large blue particles (4 mm) and 85% small red particles (2 mm) after 20 revolutions about a single axis. White dotted curves represent boundaries of two nonmixing islands predicted by the continuum model for the protocol $(57^\circ, 57^\circ, 90^\circ)$ as they would appear when flowing across the free surface. White arrow indicates the flow direction.

down to the bottom of the flowing layer, while large particles rise to the top. The small particles deposit on the static bed of particles first, while the top layer of large particles continues to flow down the free surface. As a result, small particles are deposited near the middle of the flowing layer, while large particles are deposited further downstream. This deposition pattern is reinforced through periodicity due to the tumbler shape (2D) or due to the biaxial protocol (3D). The key point is that the bottom of the flowing layer consists mostly of small particles, which in the quasi-2D tumbler is where the nonmixing islands overlap the flowing layer as shown schematically in Fig. 13(a). Consequently, small particles fall into the nonmixing islands when they segregate to the bottom of the flowing layer. Even if they segregate to the bottom of the flowing layer, where a nonmixing island is not present, they continue to be advected throughout the chaotic flow region (or via collisional diffusion), and eventually make their way into the nonmixing islands in subsequent rotations.

In contrast, the conical nonmixing structures in a 3D spherical tumbler have significant volume near the tumbler wall [Fig. 13(b)]. This means that the conical base of the nonmixing regions is located where large particles tend to segregate. As a result, the large particles tend to fill the nonmixing structures in the 3D spherical tumbler. Thus, how the particle segregation in the flowing layer coincides with the nonmixing islands determines which particles accumulate in nonmixing regions. That is, the interplay between underlying advection field and the particle segregation in the flowing layer determines the ultimate segregation pattern. Whether large particles or small particles accumulate in the nonmixing regions depends on the relative location of nonmixing regions when they pass through the flowing layer.

Another important point is that the accumulation of particles in nonmixing regions is made possible when the radial segregation is in the same plane as the mixing barriers. The segregation-driven material exchange across mixing barriers into the nonmixing regions inherently occurs in a single plane in a quasi-2D tumbler. However, the spherical tumbler is more complicated because of its 3D nature. Along with the radial transport, the large particles that accumulate into the nonmixing regions must also align with the nonmixing regions in the spanwise direction, requiring axial displacement of large particles.

In studies of single-axis rotation of a spherical tumbler partially filled with size-bidisperse mixtures [24,26,50], two different axial segregation patterns occur for a mixed initial condition depending on the fill fraction, absolute particle sizes, particle size ratio, volume fraction of large particles, and smoothness of the tumbler wall. Large particles either accumulate in a band at the equator of the tumbler, or in two bands near the poles. For the operating conditions used in this study (rotation speed 2.6 rpm and half-filled tumbler), large particles tend to accumulate at the poles when the tumbler is continuously rotated about a single axis. This is shown in a top view of the free surface after 20 single-axis revolutions in Fig. 14. The large particles experience a small axial drift velocity that gradually drives them to concentrate in the bands near the poles, consistent with previous experimental results [24,26].

Nonmixing islands predicted by the continuum model for the biaxial (two-axis) rotation protocol as they pass through the flowing layer are shown by the white dotted boundaries overlaid on the single axis experiment result in Fig. 14. The axial positions of the nonmixing islands coincide with the regions of large particle accumulation for single-axis rotation. Note that the bands formed for the single-axis rotation experiment is a steady-state result after 20 tumbler revolutions. In the biaxial experiments that we focus on in this paper, each single-axis rotation action is smaller than 90°. Thus, the axial segregation is small for each iteration, yet the axial segregation is reinforced through repeated iterations. For each single-axis action about either the z axis or x axis, the large particles segregate toward the poles and accumulate in the coincident nonmixing islands. Segregation in both the radial and spanwise directions ensures that large particles move to the free surface and toward the poles where nonmixing structures have the largest volume. When this concentrating effect due to segregation is stronger than collisional diffusion, such as in the cases of large size ratios, the segregation pattern is clear and the features have distinct boundaries as shown for large size ratios in Fig. 5. Similar to radial segregation of small particles in the quasi-2D square tumbler, both radial and axial segregation aligns the large particles with nonmixing regions in the 3D spherical tumbler. Large particles are concentrated in these regions with repeated rotations. It is precisely the

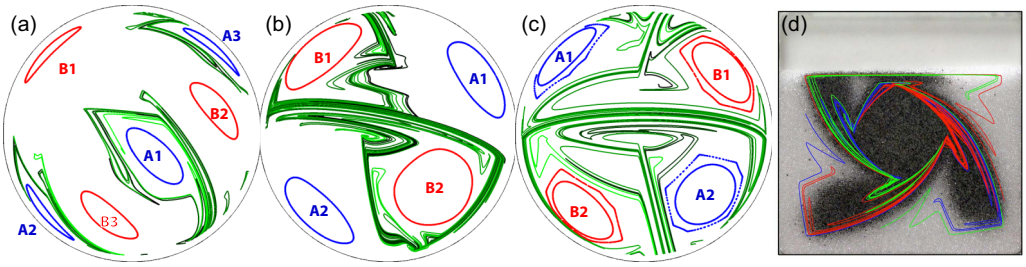

FIG. 15. Unstable manifolds of period 3 in gradient color from black (dark) to green (light) for protocol (a) (57°, 57°, 90°), (b) (90°, 90°, 80°) in (b), and (c) (90°, 90°, 90°). The blue and red closed curves (labeled as A1–A3 and B1–B3) are boundaries of nonmixing islands. Both the unstable manifolds and nonmixing islands are generated on the $r = 0.95$ surface. (d) Unstable manifolds superimposed onto experiment of a 75%-full quasi-2D tumbler with a mixture of 30% small black particles. Reprinted with permission from Meier *et al.* [8].

alignment of segregation with nonmixing regions that allows the large particles to accumulate in nonmixing regions.

B. A dynamical systems perspective

Experiments for protocols (57°, 57°, 90°), (90°, 90°, 80°), and (90°, 90°, 90°) demonstrate robust pattern formation near the tumbler wall [see Figs. 4, 5, and 11(a)–11(b)]. Particle accumulation for protocol (57°, 57°, 90°) is the most compact and has the most well-defined boundaries despite the fact that the nonmixing islands predicted by the continuum model are the smallest in size. On the other hand, the patterns for protocols (90°, 90°, 80°) and particularly protocol (90°, 90°, 90°) have less clearly defined boundaries [Figs. 11(a)–11(b)], even though the islands predicted by the continuum model are larger. This result occurs regardless of the large particle fraction, so it cannot be explained on that basis. To explore this contradiction, we examine flow behavior in the chaotic region immediately surrounding the nonmixing islands, neglecting effects of axial segregation and diffusion because they are small compared to the mean flow. The chaotic behaviors are induced by complex structures formed from stable and unstable manifolds, which correspond to contraction and expansion of material around a hyperbolic fixed point [11]. The algorithm used to compute the manifolds is described in Appendix C.

The unstable manifolds calculated from the continuum model for the portion of the tumbler visible from the bottom are shown with the nonmixing islands for protocols (57°, 57°, 90°), (90°, 90°, 80°), and (90°, 90°, 90°) in Figs. 15(a)–15(c). There are two unstable manifolds for each of the three protocols, which correspond to the two sets of periodic points. For simplicity, only one of the two manifolds is shown in Figs. 15(a)–15(c). The separate portions of the manifold shown in each of the images are connected through the flowing layer, which is not shown. As the unstable manifolds stretch from the hyperbolic points, the color progresses from black (dark) to green (light). One unstable manifold of protocol (57°, 57°, 90°) [Fig. 15(a)] wraps tightly around one group of the nonmixing islands (A1-A2-A3). Particles that happen to be bumped out of the nonmixing regions by collisional diffusion are advected by the unstable manifold. In subsequent iterations, the chance of the particle diffusing back into the nonmixing regions are high because the manifold wraps tightly around the A1-A2-A3 nonmixing regions. For protocol (90°, 90°, 80°), even though the unstable manifold wraps around the nonmixing islands B1-B2 [Fig. 15(b)], the unstable manifold linkage between the two nonmixing islands occupies a larger portion of the domain, spanning the entire tumbler horizontally. Therefore, the accumulation of large particles for protocol (90°, 90°, 80°) is less distinct [Fig. 11(a)] than for protocol (57°, 57°, 90°) [Fig. 4(a)] because a particle that starts outside of a nonmixing region or is bumped outside of the nonmixing region by collisional diffusion is more likely to be dispersed by the manifold to positions elsewhere in the chaotic region. For protocol (90°, 90°, 90°) [Fig. 15(c)], the unstable manifold spans the entire domain and forms large folds that encompass all four nonmixing islands. Thus, particles are more likely to be dispersed to regions elsewhere in the chaotic sea once they are carried away by the manifolds, as is evident in the less distinctly segregated regions for the experiment of protocol (90°, 90°, 90°) [Fig. 11(b)].

The relation between unstable manifolds and the segregation pattern is also evident in the quasi-2D tumbler. As shown in Fig. 15(d), the unstable manifolds surrounding the nonmixing islands outline the boundary of the segregation pattern. The unstable manifolds serve as a mixing barrier in that particles follow the manifolds instead of moving across them. This effect is observed in the 3D spherical tumbler for protocol (57°, 57°, 90°). In contrast, for protocol (90°, 90°, 90°), the unstable manifolds fill the entire domain, carrying particles throughout rather than acting as a barrier to mixing. As a result, the unstable manifolds in this case facilitate material transport throughout the domain, resulting in an indistinct segregation pattern [Fig. 11(b)].

VI. DISCUSSION AND CONCLUSIONS

We started this paper by asking if granular segregation and chaotic dynamics can interact in a fully 3D system to generate segregation patterns, and the answer is clearly yes based on the visualization experiments alone. To further understand the relation between the segregation and chaotic dynamics, the segregation patterns of granular flows in a 3D spherical tumbler are examined with both surface visualization and x-ray imaging. Both methods demonstrate that particles of different sizes segregate into patterns predicted by a simple kinematic continuum model, at least for the protocols

shown in this study and likely for many other protocols. The detailed characteristics of the segregation pattern depend on the relative strengths of segregation, diffusion, and chaotic advection, as is evident from experiments with different particle size ratios, mixture fractions, and rotation protocols.

The pattern formation is a result of the coincidence between the nonmixing islands of the underlying flow field and particle segregation for both the quasi-2D square tumbler studied previously [8] and the 3D spherical tumbler examined here. When the direction of accumulation due to segregation aligns with nonmixing structures of the underlying flow field, segregation patterns form.

Other factors can influence the details of the pattern, including the strength of the segregation, collisional diffusion, and unstable manifold transport. These effects can be tuned to change the pattern to various degrees. For example, the relative strength of segregation compared to diffusion can be manipulated in several ways including changing rotation speed, particle to tumbler size ratio, and relative particle sizes. For instance, the pattern becomes weak when segregation is decreased with a smaller particle size ratio and thus a higher relative influence of collisional diffusion. It is also likely that when axial segregation is weaker, manifold-driven transport becomes more important. The segregation pattern is perturbed more easily for protocol $(90^\circ, 90^\circ, 90^\circ)$ than protocol $(57^\circ, 57^\circ, 90^\circ)$, because the unstable manifolds are capable of carrying particles further away from the nonmixing regions. Hence, segregation pattern formation depends not only on the structure of dynamical systems features including elliptic nonmixing regions and unstable manifolds, but also on the relative strength of segregation compared to collisional diffusion. The relative strengths of these factors is key to predicting the pattern formation or to optimizing the mixing by avoiding such pattern formation.

It is also important to recognize that the parameter space for protocols is essentially infinite—rotation angles can vary continuously. We have described a handful of protocols in detail here, and we would expect similar results for protocols with rotation angles within a few degrees of those considered here in which similar nonmixing regions exist. We would also expect similar results for other protocols with relatively large nonmixing regions, though it would be difficult to consider the complete set of nonmixing regions that may occur [36].

In generalizing the segregation pattern formation for other protocols, several factors must be considered. As mentioned earlier, the kinematic continuum model does not include any information about the particles, and axial transport is neglected. However, as shown in Sec. V A, axial segregation occurs for size-bidisperse particles in spherical tumbler flow (however small compared to bulk flow). Thus, the possibility of unpredicted pattern formation exists as a result of the additional axial transport that is not included in the present kinematic model. The final segregation pattern depends on a complex interplay between segregation, the flow field, and diffusion. We are also conducting discrete element method simulations to verify the mechanism with a statistical approach as well as examining secondary transport in the system.

Furthermore, the 3D flow in this study generates 2D invariant structures on hemispherical shells. Therefore, radial transport occurs only via diffusion and segregation. Fully 3D transport including radial transport can occur via streamline jumping [28,38], which can be introduced to the experiments, for example, by rotating the tumbler about two axes at different speeds. Thus, 3D spherical tumbler flow can serve as a prototypical system for studying pattern formation and mixing in even more complicated 3D dynamical systems.

ACKNOWLEDGMENTS

M.Y. thanks Lachlan D. Smith for valuable discussions. This research was funded by NSF Grant No. CMMI-1435065.

APPENDIX A: CONTINUUM MODEL

In the continuum model [28,29], particles flow down the surface in a thin flowing layer that lies on top of nonflowing particles in the bulk that move in solid body rotation with the tumbler. The flow is simplified to two dimensional in the streamwise direction. The flowing layer velocity is approximated by a constant shear rate velocity profile. For rotation about any axis (the z axis here with x in the streamwise direction and y normal to the free surface), the nondimensionalized velocity field $\mathbf{u} = (u, v, w)$ is piecewise defined such that the flowing layer $(0 \geqslant y \geqslant -\delta)$ velocity is $\mathbf{u}_{\mathrm{fl}} = ((\delta + y)/\epsilon^2, xy/\delta, 0)$ and the bulk $(y < -\delta)$ solid body rotation velocity is $\mathbf{u}_{\mathrm{b}} = (y, -x, 0)$. The interface of the lenticular flowing layer with the bulk is located at $\delta(x, z) = \epsilon\sqrt{1 - x^2 - z^2}$, where $\epsilon = \delta(0, 0) = \sqrt{\omega/\dot{\gamma}}$ is the maximal dimensionless flowing layer depth at the center of the sphere $(x = z = 0)$ for shear rate $\dot{\gamma}$ and angular rotation velocity ω. All variables are dimensionless—lengths are normalized by the tumbler radius R_0 and the rotation time is normalized by $1/\omega$. Note that we assume the particles gain the velocity described above immediately as the tumbler starts to rotate, and stop moving instantaneously as the tumbler stops rotating. This continuum model, which includes stretching characteristic of chaotic flows [11], is parameterized by the flowing layer depth ϵ, which is set to 0.15 to match the conditions in the experiments ($\omega = 2.6$ rpm). Experiments in this work are done with the same rotation speed about both the x axis and the z axis, so that $\epsilon_x = \epsilon_z$.

APPENDIX B: POINCARÉ SECTION

Stroboscopic maps of 500 iterations are used to investigate mixing and nonmixing behaviors of the underlying flow. Positions of initial points are recorded after every iteration of biaxial rotations calculated by the continuum model. The initial conditions are points seeded on the interface between the static bed and the flowing layer before the first z-axis rotation in blue and before the first x-axis rotations in red on the same radial hemispherical shell. Piecewise analytical solutions for the differential velocity profile are derived in Ref. [28] for the bulk and flowing layer. The chaotic region manifests itself as points advected throughout the domain, e.g., Fig. 3(b), while the white elliptical regions avoided by the

tracer points represent elliptic nonmixing regions that prevent material exchange. In the 3D spherical tumbler rotated with the same speed about both the z axis and the x axis, the Poincaré section exists on invariant surfaces parametrized by the radius of hemispherical shells [28]. In other words, tracer points have trajectories that lie on the same radial surfaces they start on.

APPENDIX C: UNSTABLE MANIFOLDS

The unstable manifolds are traced by tracking points seeded on a short line segment of length $0.001R_0$ in the direction corresponding to material expansion of the hyperbolic point. Positions of tracer points are recorded after every iteration, and the resulting manifolds shown for each protocol in Fig. 15 are trajectories of tracer points advected for 15 iterations. In order to maintain a uniform density tracing in the presence of fast manifold stretching, new points are back inserted in intervals between consecutive points that are $5 \times 10^{-5}R_0$ apart or further after each iteration.

The eigenvalues and eigenvectors of the hyperbolic points are first calculated from the Jacobian of the mapping $\Phi^n(x) = x$ of the biaxial tumbler flow [28,51]. For the volume-preserving map studied here, the three eigenvalues have a product of $\lambda_1\lambda_2\lambda_3 = 1$. There is a null direction at each periodic point providing a local invariant, corresponding to the eigenvalue of 1, $\lambda_1 = 1$ [51]. A hyperbolic point also has two real eigenvalues whose product is 1, $\lambda_2 = 1/\lambda_3$. Material expands along the direction corresponding to eigenvalue $\lambda > 1$, and contracts along the direction corresponding to eigenvalue $\lambda < 1$ [52]. The unstable manifold associated with a hyperbolic point consists of all points that converge to the hyperbolic point as the number of iterations of the map approaches negative infinity.

[1] S. B. Savage and C. K. K. Lun, Particle size segregation in inclined chute flow of dry cohesionless granular solids, J. Fluid Mech. **189**, 311 (1988).

[2] V. N. Dolgunin and A. A. Ukolov, Segregation modeling of particle rapid gravity flow, Powder Technol. **83**, 95 (1995).

[3] Y. Fan, K. V. Jacob, B. Freireich, and R. M. Lueptow, Segregation of granular materials in bounded heap flow: A review, Powder Technol. **312**, 67 (2017).

[4] L. A. Golick and K. E. Daniels, Mixing and segregation rates in sheared granular materials, Phys. Rev. E **80**, 042301 (2009).

[5] K. M. Hill, D. V. Khakhar, J. F. Gilchrist, J. J. McCarthy, and J. M. Ottino, Segregation-driven organization in chaotic granular flows, Proc. Natl. Acad. Sci. USA **96**, 11701 (1999).

[6] D. V. Khakhar, J. J. McCarthy, J. F. Gilchrist, and J. M. Ottino, Chaotic mixing of granular materials in two-dimensional tumbling mixers, Chaos **9**, 195 (1999).

[7] S. J. Fiedor and J. M. Ottino, Mixing and segregation of granular matter: Multi-lobe formation in time-periodic flows, J. Fluid Mech. **533**, 223 (2005).

[8] S. W. Meier, S. E. Cisar, R. M. Lueptow, and J. M. Ottino, Capturing patterns and symmetries in chaotic granular flow, Phys. Rev. E **74**, 031310 (2006).

[9] S. W. Meier, R. M. Lueptow, and J. M. Ottino, A dynamical systems approach to mixing and segregation of granular materials in tumblers, Adv. Phys. **56**, 757 (2007).

[10] G. Haller and G. Yuan, Lagrangian coherent structures and mixing in two-dimensional turbulence, Phys. D Nonlinear Phenom. **147**, 352 (2000).

[11] J. M. Ottino, *The Kinematics of Mixing: Stretching, Chaos, and Transport* (Cambridge University Press, Cambridge, 1989).

[12] J. Mellmann, The transverse motion of solids in rotating cylinders-forms of motion and transition behavior, Powder Technol. **118**, 251 (2001).

[13] H. Henein, J. K. Brimacombe, and A. P. Watkinson, Experimental study of transverse bed motion in rotary kilns, Metall. Trans. B **14**, 191 (1983).

[14] S. H. Strogatz, *Nonlinear Dynamics and Chaos* (Westview Press, Boulder, 2001), p. 512.

[15] K. M. Hill and J. Kakalios, Reversible axial segregation of binary mixtures of granular materials, Phys. Rev. E **49**, R3610 (1994).

[16] K. M. Hill, G. Gioia, D. Amaravadi, and C. Winter, Moon patterns, sun patterns, and wave breaking in rotating granular mixtures, Complexity **10**, 79 (2005).

[17] N. Jain, J. M. Ottino, and R. M. Lueptow, Regimes of segregation and mixing in combined size and density granular systems: An experimental study, Granul. Matter **7**, 69 (2005).

[18] I. Zuriguel, J. M. N. T. Gray, J. Peixinho, and T. Mullin, Pattern selection by a granular wave in a rotating drum, Phys. Rev. E **73**, 061302 (2006).

[19] S. W. Meier, D. A M. Barreiro, J. M. Ottino, and R. M. Lueptow, Coarsening of granular segregation patterns in quasi-two-dimensional tumblers, Nat. Phys. **4**, 244 (2008).

[20] O. Zik, D. Levine, S. G. Lipson, S. Shtrikman, and J. Stavans, Rotationally Induced Segregation of Granular Materials, Phys. Rev. Lett. **73**, 644 (1994).

[21] I. S. Aranson and L. S. Tsimring, Dynamics of Axial Separation in Long Rotating Drums, Phys. Rev. Lett. **82**, 4643 (1999).

[22] K. Choo, M. W. Baker, T. C. A. Molteno, and S. W. Morris, Dynamics of granular segregation patterns in a long drum mixer, Phys. Rev. E **58**, 6115 (1998).

[23] T. Finger, F. von Rüling, S. Lévay, B. Szabó, T. Börzsönyi, and R. Stannarius, Segregation of granular mixtures in a spherical tumbler, Phys. Rev. E **93**, 032903 (2016).

[24] U. D'Ortona, N. Thomas, and R. M. Lueptow, Influence of rough and smooth walls on macroscale granular segregation patterns, Phys. Rev. E **93**, 022906 (2016).

[25] P. Chen, J. M. Ottino, and R. M. Lueptow, Granular axial band formation in rotating tumblers: A discrete element method study, New J. Phys. **13**, 055021 (2011).

[26] P. Chen, B. J. Lochman, J. M. Ottino, and R. M. Lueptow, Inversion of Band Patterns in Spherical Tumblers, Phys. Rev. Lett. **102**, 148001 (2009).

[27] G. Juarez, R. M. Lueptow, J. M. Ottino, R. Sturman, and S. Wiggins, Mixing by cutting and shuffling, Europhys. Lett. **91**, 20003 (2010).

[28] I. C. Christov, R. M. Lueptow, J. M. Ottino, and R. Sturman, A study in three-dimensional chaotic dynamics: Granular flow and transport in a bi-axial spherical tumbler, SIAM J. Appl. Dyn. Syst. **13**, 901 (2014).

[29] Z. Zaman, M. Yu, P. P. Park, J. M. Ottino, R. M. Lueptow, and P. B. Umbanhowar, Persistent structures in a three-dimensional dynamical system with flowing and non-flowing regions, Nat. Commun. **9**, 3122 (2018).

[30] G. Juarez, I. C. Christov, J. M. Ottino, and R. M. Lueptow, Mixing by cutting and shuffling 3D granular flow in spherical tumblers, Chem. Eng. Sci. **73**, 195 (2012).

[31] Thomas F. Lynn, Julio M. Ottino, and Paul B. Umbanhowar, Cutting and shuffling a hemisphere: Nonorthogonal axes, Phys. Rev. E **99**, 032204 (2019).

[32] A. Goetz, Dynamics of a piecewise rotation, Discret. Contin. Dyn. Syst. **4**, 593 (1998).

[33] A. Goetz, Dynamics of pievewise isometries, Illinois J. Math. **44**, 465 (2000).

[34] R. Sturman, The role of discontinuities in mixing, Adv. Appl. Mech. **45**, 51 (2012).

[35] J. H. B. Deane, Piecewise isometries: Applications in engineering, Meccanica **41**, 241 (2006).

[36] P. P. Park, P. B. Umbanhowar, J. M. Ottino, and R. M. Lueptow, Mixing with piecewise isometries on a hemispherical shell, Chaos **26**, 073115 (2016).

[37] L. D. Smith, P. P. Park, P. B. Umbanhowar, J. M. Ottino, and R. M. Lueptow, Predicting mixing via resonances: Application to spherical piecewise isometries, Phys. Rev. E **95**, 062210 (2017).

[38] I. C. Christov, J. M. Ottino, and R. M. Lueptow, From streamline jumping to strange eigenmodes: Bridging the Lagrangian and Eulerian pictures of the kinematics of mixing in granular flows, Phys. Fluids **23**, 103302 (2011).

[39] M. Yu, P. B. Umbanhowar, J. M. Ottino, and R. M. Lueptow, Cutting and shuffling of a line segment: Effect of variation in cut location, Int. J. Bifurc. Chaos **26**, 1630038 (2016).

[40] POV-Ray, the persistence of vision raytracer, http://www.povray.org/ (cited May 2019).

[41] P. Mullowney, K. Julien, and J. D. Meiss, Blinking rolls: Chaotic advection in a three-dimensional flow with an invariant, SIAM J. Appl. Dyn. Syst. **4**, 159 (2005).

[42] Z. Pouransari, M. F. M. Speetjens, and H. J. H. Clercx, Formation of coherent structures by fluid inertia in three-dimensional laminar flows, J. Fluid Mech. **654**, 5 (2010).

[43] N. R. Moharana, M. F. M. Speetjens, R. R. Trieling, and H. J. H. Clercx, Three-dimensional Lagrangian transport phenomena in unsteady laminar flows driven by a rotating sphere, Phys. Fluids **25**, 093602 (2013).

[44] See Supplemental Material at http://link.aps.org/supplemental/10.1103/PhysRevE.99.062905 for figures showing the persistence, repeatability, and similarity of segregation patterns.

[45] Y. Fan, Y. Boukerkour, T. Blanc, P. B. Umbanhowar, J. M. Ottino, and R. M. Lueptow, Stratification, segregation, and mixing of granular materials in quasi-two-dimensional bounded heaps, Phys. Rev. E **86**, 051305 (2012).

[46] J. Crocker and D. Grier, Methods of digital video microscopy for colloidal studies, J. Colloid Interf. Sci. **179**, 298 (1996).

[47] N. Nityanand, B. Manley, and H. Henein, An analysis of radial segregation for different sized spherical solids in rotary cylinders, Metall. Trans. B **17**, 247 (1986).

[48] S. M. Pizer, E. P. Amburn, J. D. Austin, R. Cromartie, A. Geselowitz, T. Greer, B. ter Haar Romeny, J. B. Zimmerman, and K. Zuiderveld, Adaptive histogram equalization and its variations, Comput. Vision, Graph. Image Process. **39**, 355 (1987).

[49] K. Zuiderveld, Contrast limited adaptive histogram equalization, in *Graphics Gems IV*, edited by P. Heckbert (Academic Press, New York, 1994), pp. 474–485.

[50] L. Naji and R. Stannarius, Axial and radial segregation of granular mixtures in a rotating spherical container, Phys. Rev. E **79**, 031307 (2009).

[51] L. D. Smith, M. Rudman, D. R. Lester, and G. Metcalfe, Bifurcations and degenerate periodic points in a three dimensional chaotic fluid flow, Chaos **26**, 053106 (2016).

[52] J. Moser, *Stable and Random Motions in Dynamical Systems* (Princeton University Press, Princeton, 1973).